Modelling and Control of Multi-terminal MVDC Distribution Network

Patrobers Simiyu†, IEEE Student Member; Ai Xin IEEE, Senior Member; Lawrence Bibaya; IEEE Student; Vedaste Ndiyishimiye; George Adwek, Girmaw T. Bitew,

Abstract—**The revolution in the power industry has motivated a paradigm shift in the multi-terminal voltage source converter (VSC) medium voltage DC (MVDC) distribution network application from ship to power grid with numerous market-based applications. However, research in MVDC networks in the power grid is in its embryonic stages, hence exploring the existing primary control schemes in the well-developed VSC-HVDC systems as the benchmark for adoption remains an interesting research subject. Therefore, this paper proposes a 10kV radial multi-terminal MVDC distribution network in PSCAD/EMTDC with solar PV integrated and a preliminary study involving modelling and comparison of the master-slave, voltage margin and droop control schemes undertaken. The results show that the droop control is the most responsive and flexible achieving the best network DC voltage control and active power balance in the MVDC distribution network. The growing research interests in MVDC control provides an impetus into future study on adaptive droop control schemes..**

Index Terms—**MVDC distribution network, master-slave, voltage margin, droop control, primary level control.**

I. INTRODUCTION

THE liberalization and climate change mitigation in the power industry has motivated a paradigm shift in the multi-terminal voltage source converter (VSC) medium voltage DC (MVDC) distribution network application from ship to the power grid[1],[2]. These has driven the need for MVDC distribution network for de-risking VSC-HVDC transmission networks, AC distribution network reinforcement, transmission/distribution level renewable energy (RE) integration, rail transport applications as well as urban and rural electrification[3],[4],[5]. Unlike the conventional medium voltage AC (MVAC) system, the MVDC distribution system constitutes fewer power conversion stages making it more efficient presenting high prospects for future development hence proposed as an alternative to the AC distribution in commercial and industrial applications [1]-[6].

MVDC distribution system typically rated 1.5-30kV, may consist of intermittent RE and variable loads in a diverse system topology[7],[8],. The grid can be radial or mesh similar to the MVAC distribution. In the radial topology, each converter is connected to a central node. Its availability is lower in case the central node fails as the entire network collapses. In contrast, the mesh structure has converters connected in a ring architecture enabling power to flow from both ends of every node hence improving reliability. These features significantly impacts on the system stability and security hence the need for appropriate coordinated control strategy[9]. In multi-terminal MVDC grids, the DC voltage is directly related to the power balance and power flow similar to the AC frequency in AC system thus the DC voltage coordinated control is fundamental in the operation and stability of the multi-terminal DC (MTDC) grid [9],[10].

Research in MVDC distribution networks is in its infancy stage, thus the question of whether or not the existing control schemes in VSC-HVDC are applicable to the MVDC is a subject for exploration[11]. The master-slave and DC voltage droop control are the most fundamental DC voltage control strategies in the MTDC HVDC systems. In addition, the voltage margin is typically a modification of the master-slave control method[10].

In the master-slave strategy, one converter terminal (master) regulates the DC voltage in constant DC voltage mode while the others (slaves) are configured in constant power or AC voltage modes. The master controls the DC bus voltage and distributes power references to the slaves using a communication system. It is the simplest in design as well as in implementation and has high dynamic response/controllability with little risk of undesirable interaction between various voltage regulators. However, an outage of the master terminal can result in over-voltage/under voltage and subsequent collapse of the entire grid. The control scheme also needs accurate and high speed communication system between the converter terminals for coordinating the control scheme. In addition, the master terminal power rating should be adequately large and the connected host AC system sufficiently strong to accommodate possible power imbalances in the MTDC grid[12],[13],[14]. The practicability of the master-slave control declines with increase in the network size hence the strategy lacks the N-1 security as it can easily lose any one of its N components and stop operating [10].

The voltage margin method undertakes the DC voltage control in which the constant power and constant DC voltage

---

P. Simiyu, Ai Xin, L. Bibaya, B. T Garmaw, V. Ndiyishimiye, E. Mohammed and W. Kunyu are with the North China Electric Power University; Beijing 102206, China (simiyupr@yahoo.com).

G. Adwek, is with the Hebei University of Technology; Tianjin, 300130, China

978-1-5386-6461-2/18/$31.00 ©2018 IEEE

modes are combined in each converter terminal. The DC voltage reference value of each terminal differs by a given margin and the voltage control priority given to the terminal with the lowest voltage reference. The primary DC voltage control in the MTDC grid is transferred from one terminal with the smallest reference to the others with the largest in a cascading way[9],[15]. This method is highly reliable as the DC voltage working point is fixed and it is possible to precisely control the power flow in the MTDC grid. However, as one converter terminal controls the DC voltage at a time, it is vulnerable to unsatisfactory transient performance especially in a large network. Additionally, when the number of terminals increase, configuring their voltage margins to satisfy the steady-state and dynamic grid requirements is challenging besides its slow dynamic response[15],[16].

In the DC voltage droop control, the droop controller is configured in each terminal to enable the voltage control task in the MTDC grid to be distributed amongst the converter terminals [15]. It is considered the most reliable as the grid can't collapse even when one voltage controlling converter fails after a severe contingency as the remaining terminals share the voltage control responsibility by adjusting their power being absorbed in line with the voltage deviation. Besides, it is easy to configure the droop control scheme without rigorously modifying the control system of the other converters. Moreover, many terminals can be incorporated with the droop controller to form a large MTDC grid and enhance stability and reliability without the need for fast communication system[9]-[13]. The main drawback of the droop control method is derived from the inherent trade-off between the DC voltage deviations and the power sharing accuracy. The DC voltage working point in the droop strategy is not fixed hence the power flow can't be controlled precisely[17],[18]. Consequently, many adaptive droop control methods have been proposed in literature to simultaneously and effectively fulfil the constraints on DC voltage and power deviations[16],[18],[19],[20].

As interests in MVDC distribution networks increase, the DC voltage control methods previously popular in the HVDC systems become the reference point for investigations. Therefore, this paper proposes a 10kV radial multi-terminal MVDC network in PSCAD/EMTDC with solar PV integrated and a preliminary study involving modelling and comparison of the master-slave, voltage margin and droop control schemes undertaken at primary level. The network dynamic models are shown in. Fig. 1.0.

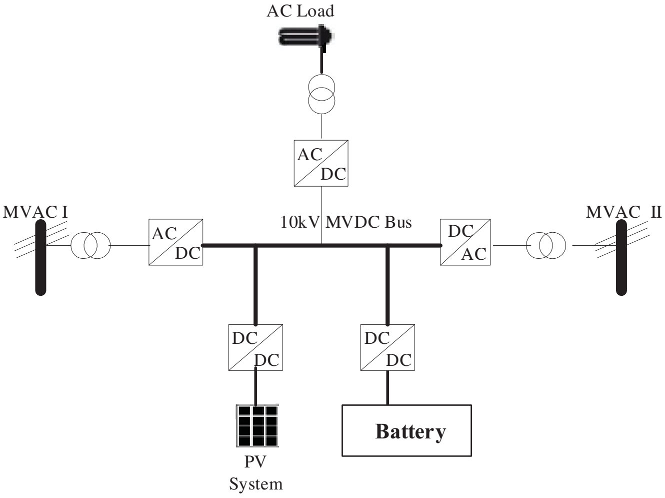

Fig.1. The Multi-terminal MVDC Distribution Network Model

II. MULTI-TERMINAL MVDC DISTRIBUTION NETWORK DYNAMIC MODELS

The modeling concepts of each of the multi-terminal MVDC distribution network model in Fig. 1.0 are outlined prior to assembly and validation in PSCAD/EMTDC.

A. *Three-Level VSC NPC*

The three phase 3-level VSC neutral point clamp (NPC) power converter topology is chosen for the MVDC distribution network. This topology is attractive because its control system and modulation scheme are simple to implement. The 3-level NPC has lower total harmonic distortion (THD) than the conventional 2-level VSC which minimizes the network filtering needs [21]. The absence of dynamic voltage sharing problems is the main reasons that places the 3-level VSC practically higher on the market for medium voltage and high power applications [22].

The NPC VSC can be applied separately as a rectifier and inverter when connected to an AC power source and load respectively. On the other hand, it can serve as an integral bidirectional AC-DC power conversion equipment [23]. All the three configurations of the three phase 3-level NPC converters are identical hence the discussion focuses on the DC-AC converter from which the operation of the others will be instinctive. A typical 3-level half-bridge (HB) VSC NPC consists of a series connection of two 2-level HBs as switching sets with some minor modifications per phase leg as shown in Fig. 2. The two HBs are connected via two clamping diodes per phase that form the neutral point that divides the DC link into two equal halves each equipped with a DC capacitor. Each phase comprise three switching states in which two control signals are complimentary to avoid short-circuiting the DC link. The gating signals are binary in nature with ‘1’ and ‘0’ when the switch is ‘ON’ and ‘OFF’ respectively as shown in Fig. 2.

To coordinate the two 2-level HBs and control the average value of the terminal voltage, the pulse-width modulation (PWM) scheme is applied to control the duty ratios of the HBs [16],[23].

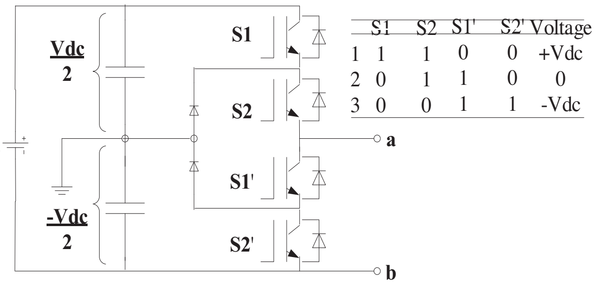

	S1	S2	S1'	S2'	Voltage
1	1	1	0	0	+Vdc
2	0	1	1	0	0
3	0	0	1	1	-Vdc

Fig. 2. 3-Level VSC NPC Phase Leg

In the MVDC network in Fig. 1, the VSC NPC is connected to the MVAC I through a reactor and an AC transformer. The inner and outer controllers for the VSC primary control system are shown in Fig. 3. The space-phasor of the AC side of the VSC-based system is expressed in terms of the dq-axis components created by the phase locked loop (PLL). The PLL synchronizes the input and output signals' phase and frequency by fixing its output signal to be in step with the AC grid voltage.

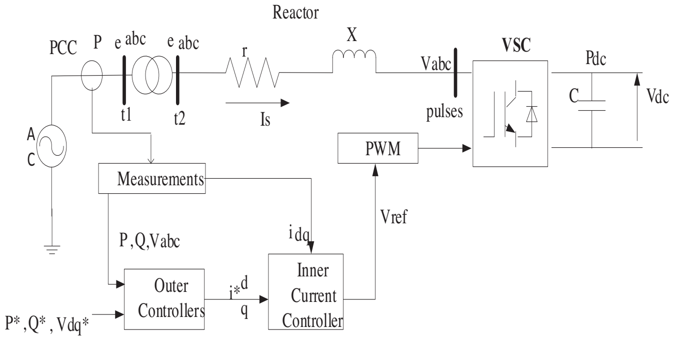

Fig. 3. VSC NPC Control

Inner Current Controller

The dynamic equations in three phase stationary coordinate system describing the VSC system behavior based on the Kirchoff's Voltage Law (KVL) [24],[25],[26] in Fig. 3 is given in (1), where e_{abc} and v_{abc} are the AC voltages at the point of common coupling (PCC) and VSC terminal respectively.

$$e_{abc} + v_{abc} = ri_{abc} + L\frac{d}{dt}i_{abc} \tag{1}$$

Equation (1) is rewritten in terms of the AC-side currents in space-vector then transformed to the dq frame in (2) assuming steady-state operation conditions. The PLL ensures that its output signal is in phase with the AC grid voltage input. In this case, the d-axis of the dq frame is locked with the AC voltage, *e* at the PCC to realize a decoupled control of active and reactive power. This represents a two input-output dynamic system where i_{dq} are state variables, v_{dq} are control inputs and e_{dq} the disturbance inputs.

$$L\frac{d}{dt}i_{dq} = e_{dq} - v_{dq} - ri_{dq} \pm j\omega L \tag{2}$$

Taking the Laplace Transform, the output current is obtained in (3).

$$\begin{aligned} sLi_d &= e_d - v_d - ri_d + j\omega Li_q \\ sLi_q &= e_q - v_q - ri_q - j\omega Li_d \end{aligned} \tag{3}$$

The d and q axes components are respectively cross coupled due to the cross terms ωLi_q and ωLi_d. Therefore, a feed-forward compensator is provided for independent control of the dq axes. Two identical *d* and *q* axes closed loop inner current controller with a proportional integral (PI) controller for excellent performance is shown in Fig. 4.

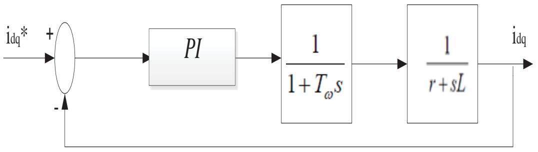

Fig. 4 Simplified Closed-Loop Inner Current Controller

The main objective of the inner controller is to regulate i_{dq} to the corresponding references i^*_{dq}. The converter delay due to the PWM is incorporated where Tω is the switching delay related to the switching frequency (f_s) given in (4). K_p and K_i are proportional and integral gains respectively.

$$T_\omega = \frac{1}{2f_s} \tag{4}$$

The loop gain l(s) is given in (5) whose pole is very close to the origin. This signifies a trend in which l(s) begins to drop from a relatively low frequency. Thus, the pole is cancelled by a compensator zero given as $s=(-k_i/k_p)$ then the system's closed loop transfer first order function is given as (6).

$$l(s) = \left(\frac{K_p}{Ls}\right)\frac{s + {}^{k_i}\!/_{k_p}}{s + {}^{r}\!/_{L}} \tag{5}$$

$$G_i(s) = \frac{I_d(s)}{I_{dref}(s)} = \frac{1}{\tau_i s + 1} \tag{6}$$

where $k_p=L/\tau_i$ and $k_i=r/\tau_i$ while τ_i is the closed-loop system's time constant which is a design choice. As a rule of thumb, the time constant should be small i.e 0.5-5ms for fast response of the inner current controller [23].

To ensure a fast dynamic response of the inner current controllers, the modulus optimum technique was used for tuning its PI parameters in the study because of its simplicity and fast response. Based on [27],[28], the modulus optimum technique involves pole cancellation and optimization of the absolute value to unity. This technique is effectively used when tuning PI controllers in the control system with one dominant time constant and the other minor time constant by cancelling the largest time constant while the closed loop gain maintains larger than unity at high frequencies.

Outer Controllers

In addition to the inner current controllers in the VSC, there are active and reactive power; DC voltage and AC voltage outer controllers. From Fig. 3, the apparent power S at the PCC is given as (7) in *dq* frame [17].

$$\begin{aligned} S &= \tfrac{3}{2} e_{dq} i_{dq}^{*} = \tfrac{3}{2}\left(e_d + je_q\right)\left(i_d - ji_q\right) \\ S &= \tfrac{3}{2}\left\{\left(e_d i_d + e_q i_q\right) + j\left(e_q i_d - e_d i_q\right)\right\} \end{aligned} \tag{7}$$

The PLL effects the transformation of the AC voltage e_{abc} at the PCC to e_{dq}. The voltage vector oriented control (VOC) is used to decouple the active and reactive power in which the it adjusts the rotational speed of the dq-axis frame such that $e_q = 0$ by aligning the e_d vector with the d-axis at steady-state. Thus, the active and reactive power injected to or absorbed from the AC system at the PCC is given in (8).

$$\begin{aligned} P &= \frac{3}{2} e_d i_d \rightarrow i_d^{*} = \frac{2P^{*}}{3e_d} \\ Q &= -\frac{3}{2} e_d i_q \rightarrow i_q^{*} = -\frac{2Q^{*}}{3e_d} \end{aligned} \tag{8}$$

Therefore, based on (8), the active and reactive power at the PCC can be controlled by i_d and i_q respectively which constitutes the PQ control mode of a VSC terminal. Fig. 5 shows the active and reactive power controllers. The controllers' outputs have limiter functions for restricting the reference currents within permissible values. The active and reactive power flow can be effectively and independently controlled by fast reference tracking of their corresponding references commands; $i_{dq} \equiv i_{dqref}$.

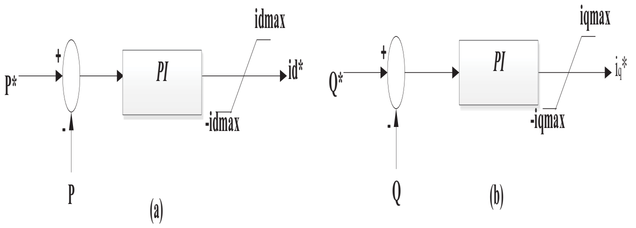

Fig.5 Active and Reactive Power Controllers

Active power can be regulated as an intermediate variable by i_d for ultimately controlling DC voltage to its corresponding reference in the DC grid. The power balance equation between the AC input and the DC-side in Fig. 3 is given in (9). The power losses of the VSC are ignored as the reactor reactance has very small resistance.

$$\begin{aligned} &P - P_{dc} - P_c = 0 \\ &\tfrac{3}{2} e_d i_d - P_{dc} - V_{dc} i_c = 0 \end{aligned} \tag{9}$$

where P, P_{dc}, and P_c are respectively the AC input power at the PCC, power entering the DC-grid and energy stored in the DC-side capacitance. The current through the DC capacitance, (i_c) is given in (10).

$$i_c = C\frac{dV_{dc}}{dt} = \left\{\frac{3e_d i_d}{2V_{dc}} - \frac{P_{dc}}{V_{dc}}\right\} \tag{10}$$

The relation expressing DC voltage is derived in (11).

$$\frac{dV_{dc}}{dt} = \frac{1}{C}\left(\frac{3e_d i_d}{2V_{dc}} - \frac{P_{dc}}{V_{dc}}\right) = \frac{3e_d}{2V_{dc}C}\left(i_d - \frac{2CP_{dc}}{3e_d}\right) \tag{11}$$

It is observed that DC voltage can be controlled the same way as active power by regulating i_d to its set point i^*_d as shown in Fig. 6. In this case, the compensator process the DC voltage error in order to determine the set point i^*_d of the inner current controller via a feed-forward compensation. The inner current controller ultimately regulates the DC voltage of the plant. The DC voltage controller alongside the reactive power controller in Fig. 5(b) forms the V_{dc}-Q control mode of a VSC terminal.

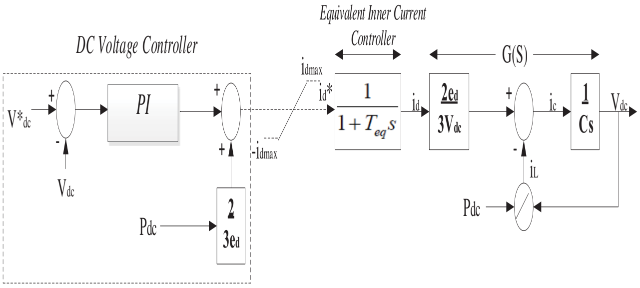

Fig. 6. VSC Controllers and the Plant

From Fig. 5 and 6, it can be observed that i_d is involved in both active power and DC voltage controllers. When the two are combined, a DC voltage droop controller is derived as shown in Fig. 7. The controller regulates the DC bus voltage linearly by changing the active power reference in proportion to the DC voltage, regulating power to its reference value simultaneously with DC voltage. The slope of the droop control characteristics is the droop constant, R_{droop} and its inverse the droop gain, K_{droop}. This parameters determine the controller sensitivity to changes in DC voltage with variations in power. With the use of the PI controller, the steady-state error of the DC voltage controller equals zero as shown in (12)[17].

$$\mathrm{P}^{*} - P + K_{droop}(V^{*} - V) = 0 \tag{12}$$

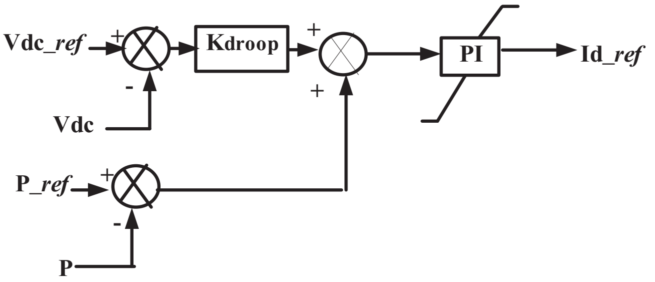

Fig. 7. DC Voltage Droop Controller

The reactive power output to or from a VSC can be regulated directly by i_q as shown in (8) or indirectly for controlling AC voltage at the PCC. From Fig. 3, (13) can be obtained between the PCC and the VSC AC terminal.

$$\bar{e} - \bar{v} = (r + j\omega L)\,\bar{i}_s \tag{13}$$

where e is the AC voltage at the PCC, v the voltage at the VSC AC terminal, r and L are respectively the reactor resistance and inductance while i_s is the AC input current at the PCC. The AC input current vector is expressed in (14).

$$\bar{i}_s = \left(\frac{S}{e}\right)^* = \left(\frac{P + jQ}{e}\right)^* = \left(\frac{P - jQ}{e}\right) \tag{14}$$

where S is the apparent power at the PCC earlier considered in (7), while P and Q are the active and reactive power respectively. The AC voltage vector at the PCC is obtained as (15).

$$\begin{aligned} \bar{e} &= \bar{v} + (r + j\omega L)\left(\frac{P - jQ}{e}\right) \\ \bar{e} &= \bar{v} + \left(\frac{\Pr + \omega LQ}{e}\right) + j\left(\frac{P\omega L - Qr}{e}\right) \end{aligned} \tag{15}$$

Considering only the real part equation (16) is realized.

$$\begin{aligned} \bar{e} &= \bar{v} + \left(\frac{\Pr + \omega LQ}{e}\right) \\ \Delta e &= \frac{\omega L}{e}\Delta Q \end{aligned} \tag{16}$$

Thus, the AC voltage at the PCC can be indirectly controlled by regulating the reactive power flow controlled by i_q as its relation with active power regulated by i_d is very weak. Thus changes in the reactive power (ΔQ) can be used to control the AC voltage at the PCC. Fig. 8 shows the AC voltage controller of a VSC terminal.

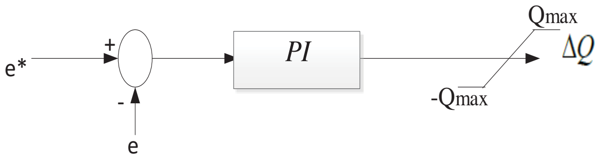

Fig. 8. AC Voltage Controller

The symmetrical optimum design criterion concepts were applied when tuning the outer controllers to obtain good stability against disturbances. The open loop transfer function with two poles at the origin like the outer controllers find this a suitable tuning approach which influences the system's frequency response to low frequencies maximizing the phase margin. Consequently, the system can tolerate more delays which optimizes the control system's behavior to disturbance input [27],[28],[29].

B. *MVAC Grid System*

The AC grid system consists of the 3-phase source, the AC bus, an ideal transformer and a phase reactor interfaced to the MVDC grid via a bidirectional 3-phase 3-level VSC NPC modelled in II(A). To enhance effective filtering of the high switching harmonics by the VSC system, an RC filter is incorporated in parallel with the reactor. The AC source supplements the distributed RES in the MVDC distribution grid. The AC system is modeled as a balanced 3-phase voltage source at 50 Hz with low internal R-L impedance. The voltage source is star-connected with neutral grounding and controls its parameters such as amplitude and frequency[30].

The primary and secondary transformers as well as converter voltages in the AC grid system are respectively given as e_{t1}, e_{t2} and V in Fig. 3. The voltage relations per phase across the reactor and the transformer are given in (17) and (18) where X and X_L are their reactance respectively [30].

$$\left[e_{t2abc} - V_{abc}\right] = \left\{\frac{X}{\omega}\frac{d(i_{abc})}{dt} + ri_{abc}\right\} \tag{17}$$

$$\left[e_{t1abc} - e_{t2abc}\right] = \frac{X_L}{\omega}\frac{d(i_{abc})}{dt} \tag{18}$$

Taking the dq transformation of (17) gives (19) and (20).

$$\left\{\frac{X}{\omega}\frac{d(i_d)}{dt} - Xi_q\right\} = \left[e_{t2d} - ri_d - V_d\right] \tag{19}$$

$$\left\{\frac{X}{\omega}\frac{d(i_q)}{dt} + Xi_d\right\} = \left[e_{t2q} - ri_q - V_q\right] \tag{20}$$

Similarly the dq transformation of (18) gives (21) and (22).

$$\left[e_{t2d} - e_{t1d}\right] = X_L i_q - \frac{X_L}{\omega}\frac{d(i_d)}{dt} \tag{21}$$

$$\left[e_{t1q} - e_{t2q}\right] = X_L i_d + \frac{X_L}{\omega}\frac{d(i_q)}{dt} \tag{22}$$

The current dynamics in the transformer in (21) and (22) are neglected. Using the PLL to align the q-axis of the dq frame with the AC system voltage at the PCC e_{t1}, then taking $e_{t1d}=0$ (23) and (24) apply.

$$e_{t2d} = X_L i_q \tag{23}$$

$$\left[e_{t1q} - e_{t2q}\right] = X_L i_d \tag{24}$$

Adding (19) and (20) to (23) and (24) respectively forms the MVAC side model equations given in (25) and (26).

$$\left\{\frac{X}{\omega}\frac{d(i_d)}{dt}-\left(X+X_L\right)i_q\right\}=\left[-ri_d-V_d\right] \quad (25)$$

$$\left\{\frac{X}{\omega}\frac{d(i_q)}{dt}+\left(X+X_L\right)i_d\right\}=\left[e_{t1q}-ri_q-V_q\right] \quad (26)$$

C. AC Load and Load-Side VSC

A constant impedance-constant current-constant power (ZIP) static AC load model is connected to the AC system's bus which in turn is linked to the MVDC grid via a 3-phase VSC NPC. It is a 3-phase block widely used for implementing a 3-phase balanced load as a series combination of RLC elements as shown in Fig. 9. The equations describing the AC load model are described in [16] using a polynomial in (27) and (28), where P_i, Q_i and V_i are the real power, active power and voltage at the i^{th} bus respectively. The variables with a 0-subscript denote the nominal values while those with 1,2 and 3 represents the fraction of the constant; Z, I and P of the AC load respectively, hence, $P_{i1}+P_{i2}+P_{i3}=1$ and $Q_{i1}+Q_{i2}+Q_{i3}=1$.

$$P_i=P_{i0}\left[p_{i1}\left(\frac{V_i}{V_{i0}}\right)^2+p_{i2}\left(\frac{V_i}{V_{i0}}\right)+p_{i3}\right] \quad (27)$$

$$Q_i=Q_{i0}\left[q_{i1}\left(\frac{V_i}{V_{i0}}\right)^2+q_{i2}\left(\frac{V_i}{V_{i0}}\right)+q_{i3}\right] \quad (28)$$

It can be observed that the active and reactive power absorbed by the ZIP load at the i^{th} bus are proportional to the square of the applied voltage. It should also be noted that at a given frequency, the AC load exhibits a constant impedance [16]. For this study, the connection configuration, the nominal voltage and frequency as well as active and reactive power are specified.

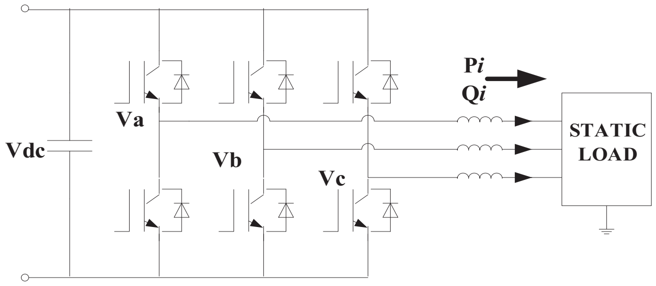

Fig. 9 Load-Side VSC NPC connected to the Fixed AC load

The mathematical model of the load-side VSC is similar to that presented in II(A). The reactive power controller in Fig. 5(b) and the AC voltage controller in Fig. 8 are used to derive the load-side AC VSC controller in Fig. 10. The load-side VSC ensures that the amplitude and frequency of the AC supply voltage to the passive AC load are constant and the PI is used to reduce the steady-state error.

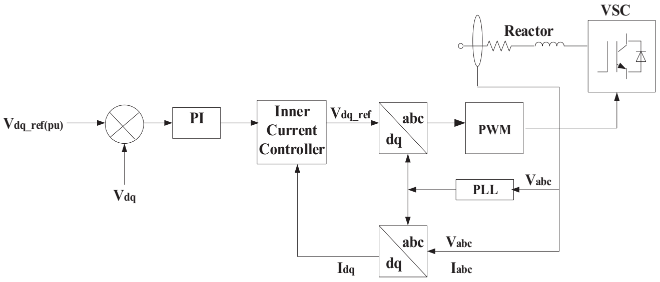

Fig. 10 Load-Side VSC Controller

D. Battery and Buck-Boost Converter

The lead-acid battery model is adopted for the study as it is the cheapest on cost per kW basis, mature and widely used battery energy source storage (BESS) technology. When analyzing the dynamic behavior of the lead acid battery, the electrical equivalent models are preferable to the mathematical and electro-chemical models. The ideal, linear and Thevenin are the common equivalent circuit models[31]. The linear model shown in Fig. 11 is the modest choice representing the battery as a voltage source with a series internal resistance [32],[33].

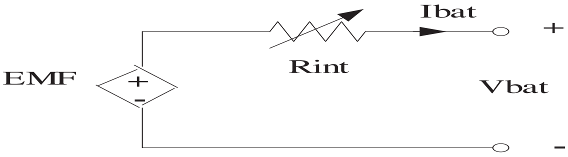

Fig.11 Linear Equivalent Circuit Model

The EMF and the internal resistance are functions of the battery state of charge (SOC) as shown in (29) and (30) while the SOC is calculated using (31). V_{min} and R_{min} are battery terminal voltage and internal resistance at the initial 0% SOC respectively while K_v and K_R are the battery constants determined by the battery type [32].

$$EMF=V_{\min}+K_vSOC \quad (29)$$

$$R_{\text{int}}=R_{\min}+K_RSOC \quad (30)$$

$$SOC=-\frac{1}{C_{\max}}\int_0^t I_{bat}(\tau)d\tau \quad (31)$$

The battery interfaces the MVDC distribution grid via the bi-directional DC-DC converter. Its charging and discharging cycles are regulated using the battery controller. The controller continually monitors the stored and the reference power as well as the corresponding voltage differences and regulates the charging and discharging regimes as shown in the flow chart in Fig. 12 [32],[34]. The constant current charging mode is recommendable for initial charging of the battery from a low SOC. As the battery terminal voltage rises to about 90% of the reference voltage, the constant voltage charging mode switches on to prevent damages arising from over charging. The acceptable voltage differences is taken as 2% [33].

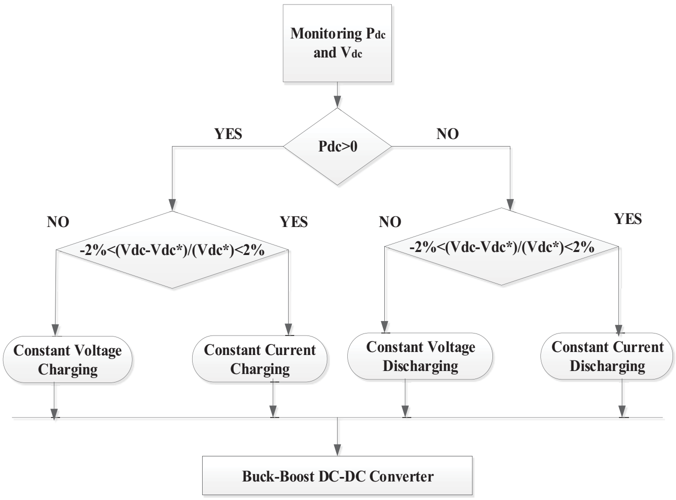

Fig. 12 Battery Control Strategy

The bidirectional DC-DC converter in Fig. 13 operates in buck-boost mode where the battery is charged from the MVDC network to its nominal SOC in the bucking mode then discharged back in the boosting mode. The actuating signals of the IGBT switches T_1 and T_2 are complementary in the PWM control mode to accordingly charge and discharge the battery [34],[35].

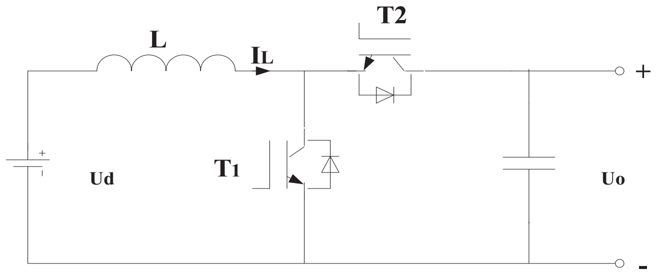

Fig. 13 Buck-Boost DC-DC Converter

Assuming a steady-state operation, the voltage across the inductor in one switching cycle is zero as given in the inductor voltage balance equation in (32) [35].

$$\int_0^{T_s} u_L dt = \int_0^{t_{on}} u_L dt + \int_{t_{on}}^{T_s} u_L dt = 0 \qquad (32)$$
$$U_d t_{on} + (-U_o) t_{off} = 0$$

where the switching period is given by Ts.

During the bucking mode, the voltage and current relations based on Lenz's Law including the average voltage and the duty cycle of the converter are given by (33), (34) and (35) respectively.

$$U_o = -L\frac{di_L}{dt} \qquad \text{....t}_{on}$$
$$U_o - U_d = -L\frac{di_L}{dt} \qquad \text{....t}_{off} \qquad (33)$$

$$L\frac{di_L}{dt} = U_o - \mathrm{DU}_d \qquad (34)$$

$$D = -\frac{1}{U_d}(U_o - \mathrm{L}\frac{di_L}{dt}) \qquad (35)$$

In the boosting mode, the voltage and current relations; the average voltage and duty cycle of the converter are given in (36), (37) and (38) respectively.

$$U_d = L\frac{di_L}{dt} \qquad \text{....t}_{on}$$
$$U_d - U_o = L\frac{di_L}{dt} \qquad \text{....t}_{off} \qquad (36)$$

$$L\frac{di_L}{dt} = U_d - \mathrm{U}_o(1 - \mathrm{D}) \qquad (37)$$

$$D = 1 - \frac{1}{U_o}(U_d - \mathrm{L}\frac{di_L}{dt}) \qquad (38)$$

where, D is the duty cycle, U_d and i_L are the battery voltage and current respectively while U_o is the MVDC bus voltage.

The control scheme of the buck and boost modes can be realized from (35) and (38) as shown in Fig. 14. In each case, the charging and discharging currents of the battery as well as the output voltages of the converter can be regulated by adjusting the converter duty cycle, D.

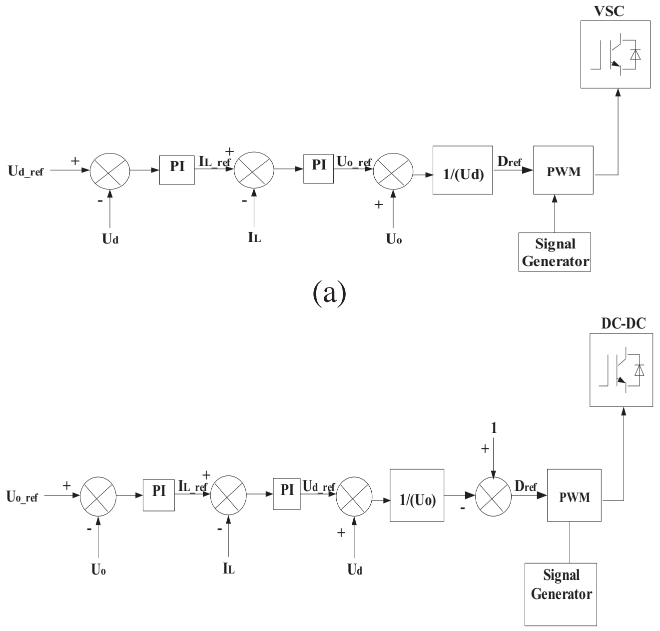

(a)

(b)

Fig. 14 Control Scheme of the buck-boost DC-DC Converter; a). Buck Mode b). Boost Mode

E. Solar PV and Boost DC-DC Converter

The solar PV is one of the fastest growing RE integrated into the distribution network. When modelling a PV system, the characteristics of the PV cell must be taken into consideration as the fundamental generator unit [36]. Typically, a PV cell delivers about 2W at 0.5V but the cells are connected in series-parallel on a PV module to generate a high amount of power. A PV array is formed with a string of modules in parallel with each string comprising series modules. The PV system output characteristics depend on the solar irradiance, the cell temperature and the output voltage [35],[37].

The performance of a PV system is usually investigated under the standard test conditions (STC) of 1000 WM^{-2} irradiance, AM 1.5 average solar spectrum and 25^{0}C cell temperature. However, since the commercial PV modules do not behave the same as in the STC in practice, appropriate PV models are employed to represent the PV systems [35]. The general equivalent PV model is moderate and most preferable [38],[37].Fig. 15 shows the general equivalent PV cell and module/array model.

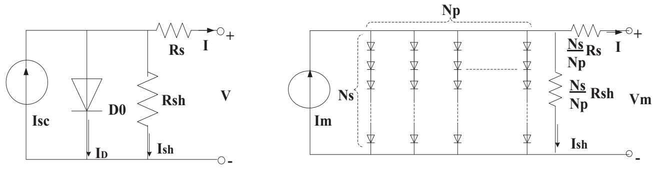

(a) (b)

Fig. 15 General Equivalent Circuit Model: a). PV Cell b). PV Module/Array

The equation for the equivalent PV cell in Fig. 15 can be derived using the basic Kirchoff's current law. The equation of the PV cell model is given in (39). The equation for a module/array configuration with N$_s$ series and N$_p$ parallel modules is adapted from [38] where (39) is modified and the subscript 'm' used to denote the module current and voltage in (40). The I$_{sc}$, I$_o$, A, N$_s$_base, R$_s$ and R$_{sh}$ represents the short circuit current, dark-saturation current, the ideality factor, original series cells, series and shunt resistances respectively. Others include the Boltzman's constant K, the elementary charge q and temperature, T. The series and parallel resistance denotes the internal cell and leakage resistance respectively. It is assumed that the photo-generated current, I$_{ph}$>>I$_o$ hence I$_{ph}$=I$_{sc}$. The combination of series and parallel modules is also accounted for in the module/array equation, where N$_p$=N$_s$=1 for a PV cell; N$_P$ =1 and N$_S$ for series number of cells in a PV module and N$_S$ and N$_P$ for series-parallel number of modules in a PV array.

$$\begin{aligned} I &= I_{sc} - I_D - I_{sh} \\ I &= I_{sc} - I_o\left[\mathrm{e}^{\frac{q(V+I\cdot R_S)}{K\cdot T\cdot A\cdot N_{s\_base}\cdot}} - 1\right] - \left[\frac{V + I\cdot R_s}{R_{sh}}\right] \end{aligned} \tag{39}$$

$$I_m = N_s\cdot I_{sc} - N_p\cdot I_o\left[\mathrm{e}^{\frac{q(V_m+I_m\cdot R_S\frac{N_S}{N_p})}{K\cdot T\cdot A\cdot N_{s\_base}\cdot N_S}} - 1\right] - \left[\frac{V_m + I_m\cdot R_s\cdot\frac{N_s}{N_p}}{R_{sh}\cdot\frac{N_s}{N_p}}\right] \tag{40}$$

The PV array output is scaled by utilizing N$_s$ and N$_p$ determined using (41); where V$_{PVmax\text{-}array}$, I$_{PVmax\text{-}array}$ and P$_{PVmax\text{-}array}$ are the maximum array voltage, current and power respectively while the I$_{mp}$ and V$_{mp}$ are respectively the maximum power current and voltage.

$$\begin{aligned} N_s &= \frac{V_{PV\max-array}}{V_{mp}} \\ I_{PV\max-array} &= \frac{P_{PVMax-array}}{N_s\ x\ V_{mp}} \\ N_p &= \frac{I_{PV\max-array}}{I_{mp}} \end{aligned} \tag{41}$$

The commercial PV manufacturers provide product datasheet for standard PV module characteristics; namely: maximum power (P$_{max}$); V$_{mp}$; I$_{mp}$; open-circuit voltage (V$_{oc}$); short-circuit current (I$_{sc}$); temperature coefficient of open-circuit voltage (K$_V$) and temperature coefficient of short-circuit current (K$_I$). This data is generally used to generate the electrical characteristics such as the current-voltage (I-V) and power voltage (P-V) curves of the PV cell/module/array [36],[39].

The maximum power point (MPP), where the operation of the entire PV system occurs at its highest efficiency typically varies under changing environmental conditions of temperature and irradiance. An MPPT system is incorporated in the boost DC-DC converter in Fig. 16. The converter operates under a control strategy similar to that in Fig. 14(b) enabling the PV system interfacing the MVDC operate at maximum efficiency.

The perturb and observe (P&O) and the incremental conductance are the most commercially employed MPPT algorithms for stand-alone and grid-interactive PV systems. However, the incremental conductance is the most preferable because of its more accurate MPPT, higher efficiency and fast convergence. The method can also track accurately even under rapidly varying environmental conditions [40],[41] hence chosen for the study.

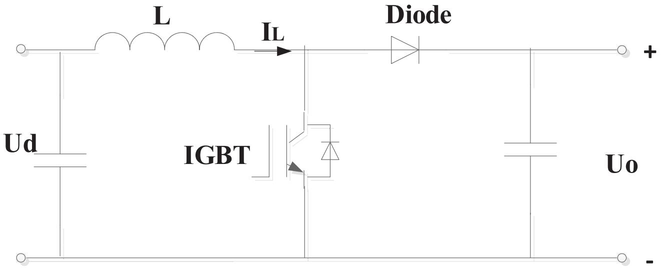

Fig. 16 DC-DC Boost Converter

The incremental conductance method is based on the slope of the P-V curve; where the slope is positive on the left of the MPP, zero at the MPP and negative on the right of the MPP as given in (42).

$$\begin{gathered}\frac{dP}{dV} > 0 \\ \frac{dP}{dV} = 0 \\ \frac{dP}{dV} < 0\end{gathered} \tag{42}$$

The incremental conductance aims to determine the voltage operating point at which the PV module instantaneous conductance equals the incremental conductance. Thus from the basic equations in (43);

$$\begin{gathered}P = VI \\ \frac{dP}{dV} = \frac{d(IV)}{dV} = I + \frac{dI}{dV} \approx I + V\frac{dI}{dV}\end{gathered} \tag{43}$$

The conditions for the true MPPT are given in (44) [42].

$$\begin{gathered}\frac{dP}{dV} = 0 \\ I + V\frac{dI}{dV} = 0 \\ \frac{dI}{dV} = -\frac{I}{V}\end{gathered} \tag{44}$$

Equation (44) indicates that the MPP can be obtained by comparing the instantaneous conductance (I/V) to the incremental conductance (dI/dV). Equations (42) and (44) can be used to derive the incremental conductance algorithm. The relations before the MPP, at the MPP and after the MPP are respectively given in (45) [41],[42].

$$\begin{gathered}\frac{dP}{dV} > 0 \quad \text{or} \quad \frac{dI}{dV} + \frac{I}{V} > 0 \\ \frac{dP}{dV} = 0 \quad \text{or} \quad \frac{dI}{dV} + \frac{I}{V} = 0 \\ \frac{dP}{dV} < 0 \quad \text{or} \quad \frac{dI}{dV} + \frac{I}{V} < 0\end{gathered} \tag{45}$$

The expressions in (45) define the three operation zones for the incremental inductance method and the flow chart is given in Fig.17. In this method, the MPP is determined by comparing the incremental conductance (IΔ/VΔ) to the PV array conductance (I/V). When (I/V = IΔ/VΔ), the output voltage at V_{ref} is the V_{MPP} and the controller maintains this voltage until the solar irradiation changes hence change in ΔI and the process is repeated. The MPPT regulates the PWM control signal of the boost converter until: $(\partial I/\partial V) + (I/V) = 0$ is satisfied by adjusting its duty cycle. In this method, the peak power of the PV array lies above 98% of its incremental conductance[40].

Fig. 17 The Incremental Conductance Method Flow Chart [41]

III. RESULTS AND DISCUSSION

A. *MVDC Distribution Network Model in PSCAD/EMTDC*

The 10kV radial MVDC distribution network in Fig. 1 is modelled and simulated in PSCAD/EMTDC. The converters at the MVAC I and II as well as that at the AC load are galvanically separated from the AC side by an equivalent transformer reactance. In the PV system, the incremental conductance algorithm is used for MPPT. The key parameters of the network are given in Table 1.

The performance of the MVDC network is assessed for master-slave, voltage margin and droop control. In the investigations, different operation situations such as start-up behavior including step changes in PV output at 2s, normal operation and operation under some contingency are considered. At t=3s and t=6s, an LLL-G fault is applied at the AC load and MVAC I respectively for 0.1s whereas at t=9s, the MVAC I is disconnected.

In the master-slave control, the MVAC I is the master while MVAC II the slave. The PV is operated at MPPT while the AC load controller regulates its terminal output voltage. At the battery, the charge controller continually monitors the charging and discharging regimes though the emphasis for the study is on the charging operation. A two-stage voltage margin controller reviewed in [10] is applied in which the DC voltage control priority is given to MVAC I where the lowest and highest DC voltage values for the margin are 9.8kV and 10.2kV respectively. The minimum, reference and maximum active power are given as -2.8MW, -3.0MW and 3.2MW respectively for MVAC II while the reference power for MVAC I is 6MW. The PV, battery and AC load controller remain the same as in the master slave control. In the droop control, the MVAC I & II are each equipped with a droop controller. A droop coefficient of 3 is used for effective sharing of the control responsibility in the network. The other converter controllers remain the same as in the master slave scheme.

TABLE 1 KEY PARAMETERS OF THE MVDC NETWORK

Parameters	Nominal Value
MVDC grid Voltage	10kV
MVDC Link Capacitance	4000μF
MVAC I/II Utility Voltage & Power	5kV; 6/3MW
Reactor Inductance (equiv. Transform.)	0.005H
AC Frequency	50Hz
PV Array Power	4MW
PV Array Equiv. Output Voltage	7kV
Boost Converter Inductance	1H
PV Capacitance	1000μF
PV-Boost side Capacitance	2500μF
Battery Voltage & Power	6kV; 0.67MW
Buck Converter Inductance	1H
Battery Side Capacitance	11000μF
AC load Voltage & Power	280V; 3MW

B. Results

Fig. 18 shows the start-up and steady-state performance features of the master-slave, voltage margin and droop control strategies. During start up, the MVDC grid voltage has a modest delay time of 0.12s, rise time of 0.19s, overshoot of 10% and settling time of 0.78s in the droop control method. The master-slave strategy closely follows with a delay time of 0.12s, a rise time of 0.22s, an overshoot of 17% and a settling time of 2s. The voltage margins registers a delay time of 0.17s, a rise time of 0.22s, an overshoot of 10% and a settling time of 1.3s. In this way, the droop control method, takes the shortest time possible for the DC voltage to be fast-tracked to the set value than the other two.

There are also startup transients mainly within the first 1s in the active power at all the terminals in the grid as expected under each control strategy with the greatest at the PV system and the loads but decay as the steady state sets in. The droop control shows the most modest start-up features closely followed by the master-slave due to faster responses than the voltage margin. The step increase in the active power output from the PV system at 2s, results in some active power decrease in the MVAC I with the master-slave and voltage margin resulting in a 3% DC voltage increase in the MVDC grid. It can be observed that the step changes have less than 1% increase in DC voltage when droop control is applied. Besides, the use of droop shows the most desirable steady-state operation where the DC voltage is highly controlled, hence the flow of active power in and out of the MVDC network.

Fig. 19 shows the contingency features for the master-slave, voltage margin and droop control strategies. When a three phase fault is applied at the AC load (t=3s), a surge in active power 5times it's nominal value occur with all the control methods. A similar effect occurs at the other converter terminals but with lower oscillation amplitudes resulting in a dip in DC voltage by 15% in the master-slave control and about 20% in both voltage margin and droop control schemes. It can be observed that the oscillations in active power and voltage after the fault are more significant on the PV output for the voltage margin. The master-slave and droop control have similar characteristics with less severe transients on the PV output. The DC voltage oscillations settle fastest after 0.5s in droop control and longest in 1.3s with the voltage margin. Similarly, the power oscillations with droop method decay fastest after 0.6s and longest in 1.2s with voltage margin.

When a three phase fault is applied at the MVAC I (t=6s), a more severe transient occur at all the network terminals under each control scheme. Dangerous power swings 20times the nominal value occurs at the battery with each of the control strategies. However, extensive power oscillations are observed on the PV system when each under master-slave and voltage margin control. Consequently the DC voltage falls to zero for master-slave and to a significantly low voltage value in voltage margin than in droop control method. The oscillations in active power especially in the PV output takes shortest to decay in 0.5-0.9s with the droop control and longest in about 2s with voltage margin. When the MVAC I (t=9s) is disconnected, a fall in active power in the network arise causing some oscillations that results in the least voltage dip of 11% when with the droop control and the largest of 15% under the voltage margin. The supply fall in MVAC I prompts more PV output with little MVAC II supplement for grid support.

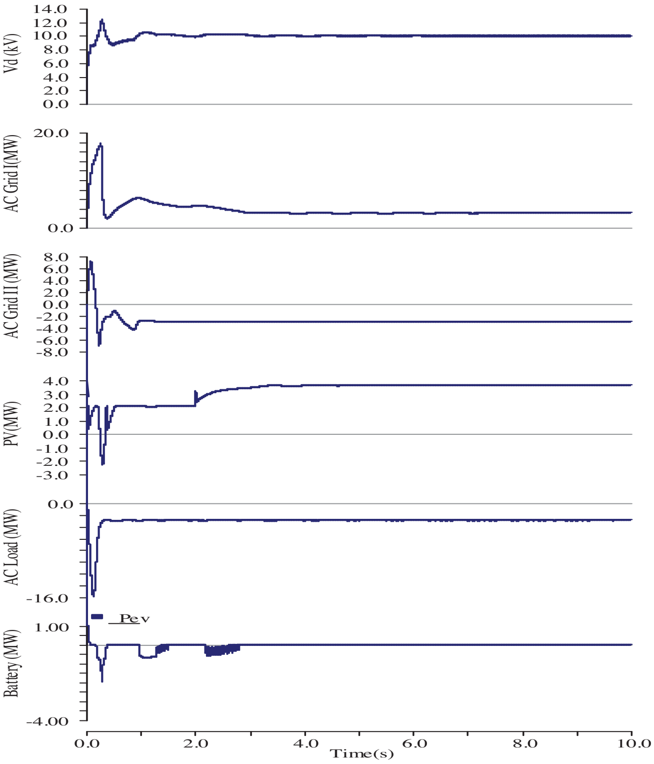

(a)

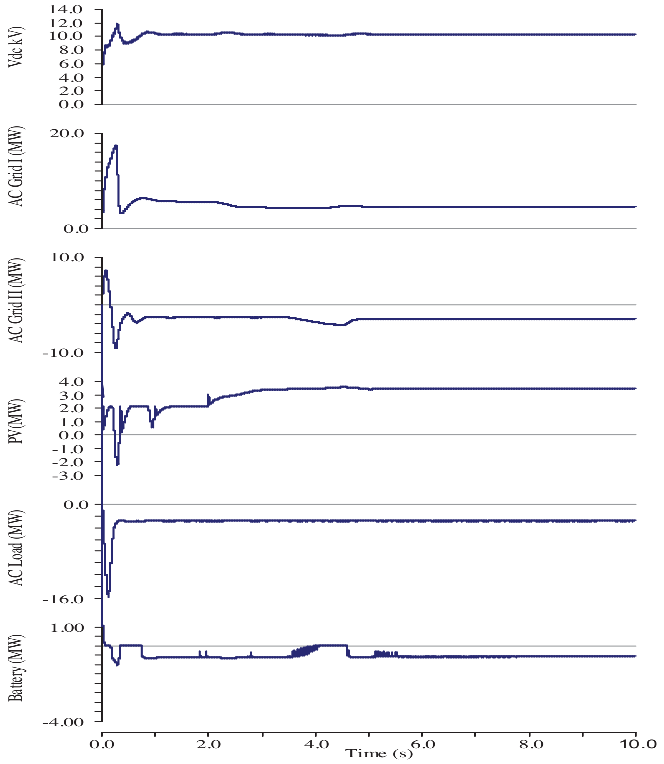

(b)

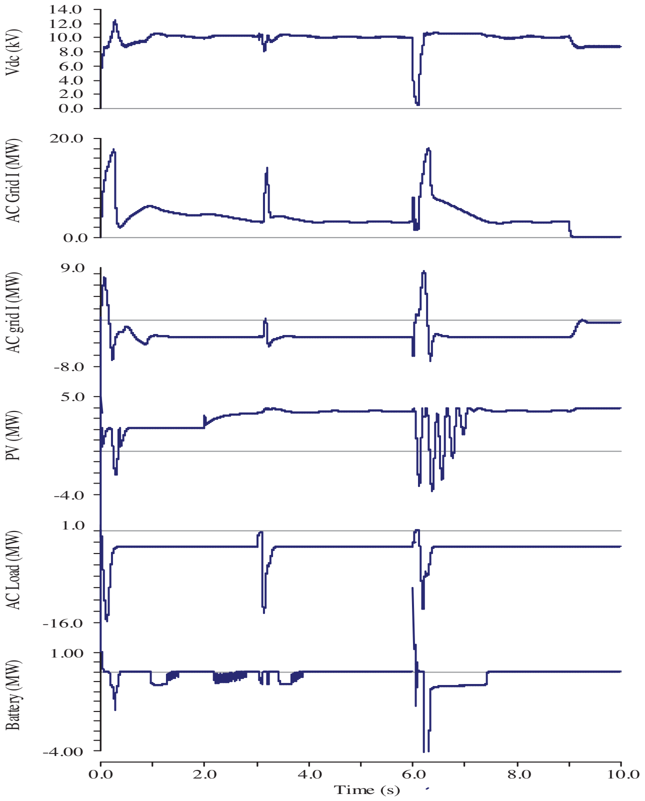

(a)

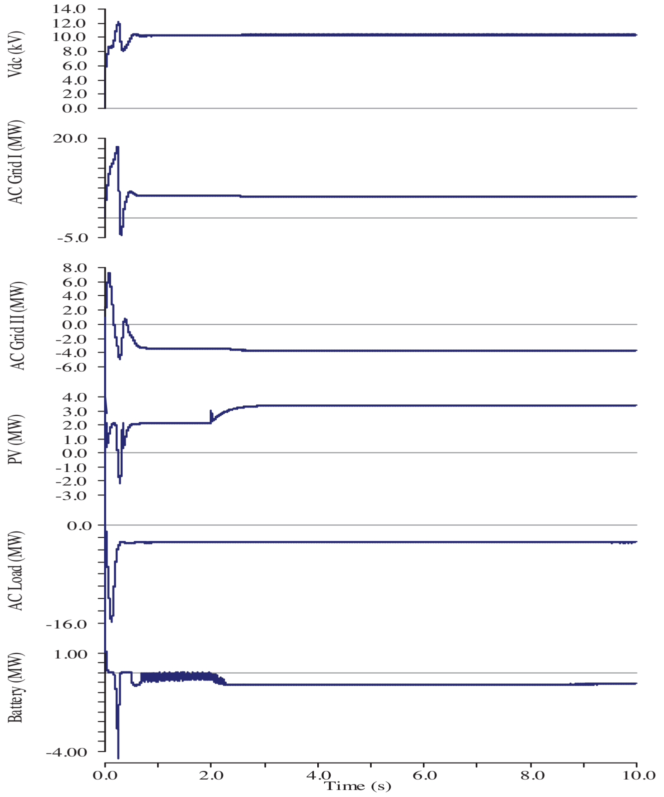

(c)

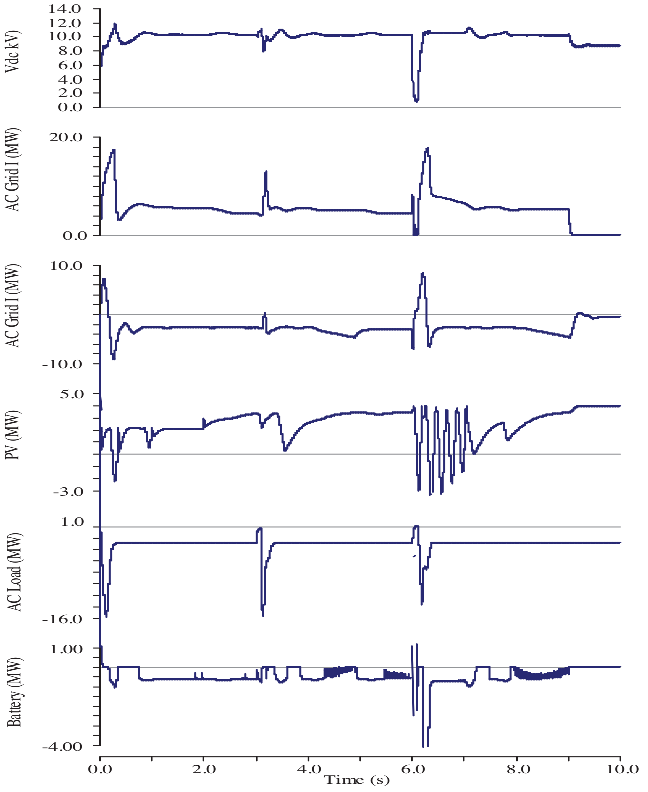

(b)

Fig. 18 Start-up and Steady-State Characteristics for: a). Master-Slave, b). Voltage Margin and c). Droop Control Strategies

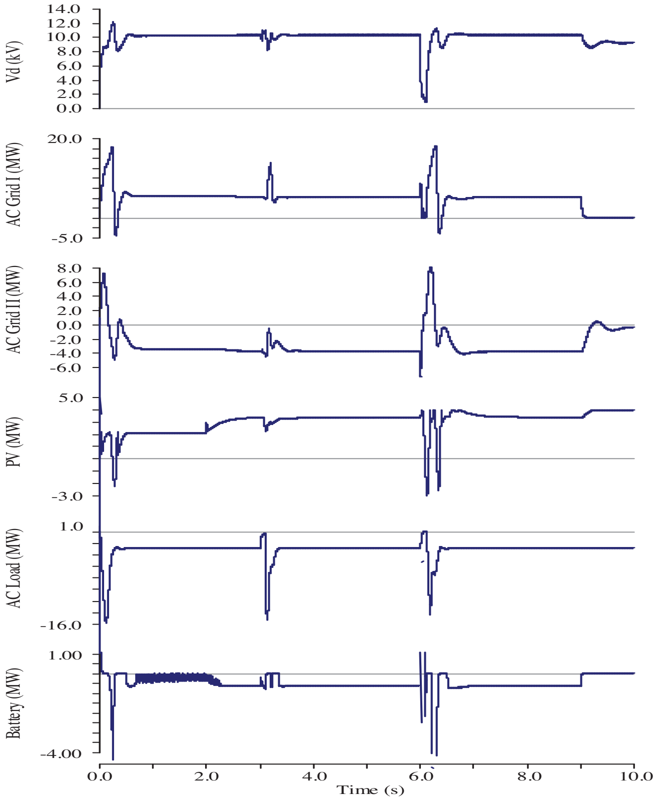

(c)

Fig. 19 Contingency Characteristics for: a). Master-Slave, b). Voltage Margin and c). Droop Control Strategies

C. Discussion

The master-slave control and voltage margin are typically centralized primary control strategies. However, the master-slave's faster response speed gives it a more competitive advantage in start-up phase with lower influences of start-up oscillations in active power and DC voltage. During steady-state operation, the two are largely similar but during transient conditions such as a three phase fault on the slack bus MVAC I, the reliability and power sharing which is a key consideration increases with the voltage margin while in the master slave decreases as the priority for DC voltage control can be shifted from the faulted converter to the other converter terminal in the network. In this MTDC grid operation, the master-slave strategy contrasting voltage margin, is too rigid to adapt to the new network changes arising from contingency scenarios.

The voltage margin and droop control depict closely related steady-state performance characteristics in which active power and DC voltage is well regulated. However, the slow response in the voltage margin causes the MVDC network to be vulnerable to the undesirable oscillatory start-up as well as persistent contingency related transients. This oscillatory control problem arises as the bandwidth of its constant DC voltage control is lower than that of the droop controller hence a longer settling time. Thus the droop control increases the MVDC distribution network dynamic response and flexibility guaranteeing better DC voltage control and active power balance.

However, the DC voltage droop strategy has its main limitation given as the inherent trade-off between DC voltage deviations and power sharing which makes precise control of active power flow challenging [17],[18]. Consequently, research in more adaptive droop control methods has emerged to simultaneously and effectively fulfil these constraints in MTDC grids. For instance, Chaudhuri et al., proposed an adaptive/variable droop scheme for effective power sharing in MTDC grids [16], [19]. A modified droop control for DC voltage restoration in MTDC system was presented by Korompili and Monti [18]. The latest proposal is the use of the fuzzy-logic based adaptive droop control in MTDC HVDC by Chen et al. [20]. From these adaptive droop proposal schemes, a better compromise between the DC voltage deviation and power sharing is made than the conventional droop control. Therefore, the adaptive droop control strategies presents great prospects for operation control of the future MTDC grid applications likely to stir greater motivation in MVDC development.

IV. CONCLUSION

The MVDC grid modelling and the comparative study of the master-slave, voltage margin and droop control of a 10kV radial multi-terminal VSC MVDC distribution network was undertaken in PSCAD/EMTDC. The results show that the MVDC network under droop control increases greatest dynamic response and adaptability that achieves the best DC voltage control and active power balance than the master-slave and voltage margin methods. The growing research interests in MVDC control motivates future study into a more adaptive droop control scheme.

ACKNOWLEDGMENT

This work was supported by 2016 National Key R & D Program of China to support Low-Carbon Winter Olympics of Integrated Smart-Grid Demonstration Project (2016YFB0900500) and the Beijing Natural Science Foundation (No.3182037)

REFERENCES

[1] G. F. Reed, B. M. Grainger, A. R. Sparacino, E. J. Taylor, M. J. Korytowski, and Z. Mao, "Medium Voltage DC Technology Developments, Applications and Trends," in Proc. 2012 *Cigre US National Committee*, pp. 1–7.

[2] G. F. Reed, B. M. Grainger, A. R. Sparacino, and Z. H. Mao, "Ship to Grid: Medium-Voltage DC Concepts in Theory and Practice," *IEEE Power Energy Mag*., vol. 10, no. 6, pp. 70–79, 2012.

[3] S. Hay, C. Cleary, G. Mcfadzean, J. Mcgray, and N. Kelly, "MVDC Technology Study-Market Opportunities and Economic Impact," 2015.

[4] M. Stieneker and R. W. De Doncker, “Medium-Voltage DC Distribution Grids in Urban Areas,” in Proc. 2016 *IEEE 7th International Symposium on Power Electronics for Distributed Generation Systems (PEDG)*, pp. 1–7.

[5] A. Darbandi, “Medium Voltage DC Distribution for Rural Electrification.” Manitoba Research Center, 2018.

[6] D. Nilsson and A. Sannino, “Efficiency Analysis of Low- and Medium-Voltage DC Distribution Systems,” in Proc. 2004 *Power Engineering Society General Meeting*, pp. 2315–2321.

[7] G. L. Kusic, G. F. Reed, J. Svensson, and Z. Wang, “A Case for Medium Voltage DC for Distribution Circuit Applications,” in Proc. 2011 *IEEE/PES Power Systems Conference and Exposition*, pp. 1–7.

[8] J. J. Mesas, L. Monjo, L. Sainz, and J. Pedra, “Study of MVDC System Benchmark Networks,” in Proc. *2015 International Symposium on Smart Electric Distribution Systems and Technologies (EDST)*, pp. 235–240.

[9] J. Binkai and W. Zhixin, “The Key Technologies of VSC-MTDC and its Application in China,” *Renew. Sustain. Energy Rev.*, vol. 62, pp. 297–304, 2016.

[10] P. Simiyu, A. Xin, G. T. Bitew, M. Shahzad, and L. K. Tuan, “A Review of the DC Voltage Coordinated Control Strategies for Multi-terminal VSC MVDC Distribution Network,” in Proc. 2018 *14th IET International Conference on AC and DC Power Transmission*, pp. 1–9.

[11] Y. Ji, Z. Yuan, J. Zhao, Y. Zhao, G. Li, and Y. Li, “Control Scheme for Multi-terminal VSC-based Medium- Voltage DC Distribution Networks,” in Proc. 2018 *14th IET International Conference on AC and DC Power Transmission*, pp. 1–8.

[12] T. K. Vrana, J. Beerten, R. Belmans, and O. B. Fosso, “A Classification of DC Node Voltage Control Methods for HVDC Grids,” *Electr. Power Syst. Res.*, vol. 103, pp. 137–144, 2013.

[13] CIGRE., “HVDC Grid Feasibility Study," (Working Group B4.52). 2013.

[14] F. Mura and R. W. De Doncker, “Design Aspects of a Medium-Voltage Direct Current (MVDC) Grid for a University Campus,” in Proc. 2011 *8th International Conference on Power Electronics - ECCE Asia*, pp. 2359–2366.

[15] R. T. Pinto, S. F. Rodrigues, P. Bauer, and J. Pierik, “Comparison of Direct Voltage Control Methods of Multi-terminal DC (MTDC) Networks through Modular Dynamic Models,” in Proc. 2011 *14th European Conference on Power Electronics and Applications*, pp. 1–10.

[16] N. R. Chaudhuri, B. Chaudhuri, R. Mujumder, and A. Yazdani, *Multi-terminal Direct Current Grids; Modeling, Analysis and Control*. New Jersey: Wiley, 2014, pp.153-168.

[17] T. M. Haileselassie and K. Uhlen, “Precise Control of Power Flow in Multiterminal VSC-HVDC using DC Voltage Droop Control,” in Proc. 2012 *Power and Energy Society General Meeting, IEEE*, pp. 1–9.

[18] A. Korompili and A. Monti, “Adaptive Droop-based Voltage Control in Multi-terminal DC Systems,” in Proc. 2017 *IEEE Manchester PowerTech*, pp. 1–7.

[19] N. R. Chaudhuri and B. Chaudhuri, “Adaptive Droop Control for Effective Power Sharing in Multi-terminal DC (MTDC) Grids,” *IEEE Trans. Power Syst.*, vol. 28, no. 1, pp. 21–29, 2013.

[20] X. Chen, L. Wang, H. Sun, and Y. Chen, “Fuzzy Logic Based Adaptive Droop Control in Multiterminal HVDC for Wind Power Integration,” vol. 32, no. 3, pp. 1200–1208, 2017.

[21] J. Rodriguez, Franquelo, L.G.G, Kouro, S. *et al.*, “Multilevel Converters: An Enabling Technology for High-Power Applications,” in *Proc. 2009 of the IEEE*, vol. 97, no. 11, pp. 1786–1817.

[22] J. Rodríguez, J. I. Leon, S. Kouro, R. Portillo, and M. A. M. Prats, “The Age of Multilevel Converters Arrives,” *IEEE Industrial Electronics Magazine*, no. 2, pp. 28–39, 2008.

[23] A. Yazdani and I. Reza, *Voltage Source Converters in Power Systems; Modeling, Control and Applications*. New Jersey: John Wiley & Sons Inc, 2010, pp.127-160.

[24] N. R. Chaudhuri, B. Chaudhuri, R. Majumder, and A. Yazdani, *Multi-terminal Direct-Current Grids; Modeling, Analysis, and Control*. New Jersey: Wiley, 2014, pp.153-168.

[25] S. Cole and R. Belmans, “A proposal for standard VSC HVDC dynamic models in power system stability studies,” *Electr. Power Syst. Res.*, vol. 81, no. 4, pp. 967–973, 2011.

[26] R. B. S. Cole J. Beerten, “Generalised Dynamic VSC MTDC Model for Power System Stability Studies,” *IEEE Trans. power Syst.*, vol. 25, no. 3, pp. 1655–1662, 2010.

[27] C. Bajracharya, M. Molinas, J. A. Suul, and T. M. Undeland, “Understanding of Tuning Techniques of Converter Controllers for VSC-HVDC,” in Proc. 2008 *Nordic Workshop on Power and Industrial Electronics (NORPIE)*.

[28] J. W. Umland and M. Safiuddin, “Magnitude and Symmetric Optimum Criterion for the Design of Linear Control Systems: What is it and How Does it Compare with the Others?,” *IEEE Trans. Ind. Appl.*, vol. 26, no. 3, 1990.

[29] M. Machaba and M. Braae, “Explicit Damping Factor Specification in Symmetrical Optimum Tuning of PI Controllers,” in Proc. 2003 *First African Control Conference.*, pp. 399–404.

[30] M. Imhof and G. Andersson, “Dynamic Modeling of a VSC-HVDC Converter,” in Proc. 2013 *48th International Universities’ Power Engineering Conference (UPEC)*, pp. 1–6.

[31] Y. H. Kirn and H. D. Ha, “Design of interface circuits with electrical battery models,” *IEEE Trans. Ind. Electron.*, vol. 44, no. 1, pp. 81–86, 1997.

[32] A. R. Sparacino, B. M. Grainger, R. J. Kerestes, and G. F. Reed, “Design and Simulation of a DC Electric Vehicle Charging Station Connected to a MVDC Infrastructure,” in Proc. 2012 *IEEE Energy Conversion Congress and Exposition (ECCE)*, pp. 1168–1175.

[33] Z. Wang, X. Li, G. Li, M. Zhou, and K. L. Lo, “Energy storage control for the photovoltaic generation system in a micro-grid,” in Proc. 2010 *5th International Conference on Critical Infrastructure*, pp. 1–5.

[34] M. Han and S. Yao, *Principles of Power Electronics*. Beijing: North China Electric Power University Press, 2015, pp.161-199.

[35] S. Arno, J. Klaus, I. Olindo, V. S. Rene, and Z. Miro, *Solar Energy; The physics and Engineering of Photovoltaic Conversion, Technologies and Systems*. Cambridge: UIT Cambridge Ltd, 2016.

[36] SMA: “Planning of a PV Generator,” pp. 1–37, 2013.

[37] H. Tsai, C. Tu, and Y. Su, “Development of Generalized Photovoltaic Model Using MATLAB / SIMULINK,” in Proc. 2008 *World Congress on Engineering and Computer Science (WCECS)*.

[38] M. . Villalva, J. . Gazoli, and E. . Filho, “Comprehensive Approach to Modeling and Simulation of Photovoltaic Arrays,” *IEEE Trans. Power Electron.*, vol. 24, no. 5, pp. 1198–1208, 2009.

[39] R. P. Sera D Teodorescu R, “PV panel model based on datasheets values,” *IEEE Transactions on Power Electronics*, 2007, vol. 4, pp. 2392–2396.

[40] T. Esram and P. L. Chapman, “Comparison of photovoltaic array maximum power point tracking techniques,” *IEEE Trans. Energy Convers.*, vol. 22, no. 2, pp. 439–449, 2007.

[41] P. Joshi and S. Arora, “Maximum power point tracking methodologies for solar PV systems – A review,” *Renew. Sustain. Energy Rev.*, vol. 70, pp. 1154–1177, 2017.

[42] D. Verma, S. Nema, A. M. Shandilya, and S. K. Dash, “Maximum power point tracking (MPPT) techniques: Recapitulation in solar photovoltaic systems,” *Renew. Sustain. Energy Rev.*, vol. 54, pp. 1018–1034, 2016.